

Flux Qubits with Long Coherence Times for Hybrid Quantum Circuits

M. Stern^{1,*}, G. Catelani², Y. Kubo¹, C. Grezes¹, A. Bienfait¹, D. Vion¹, D. Esteve¹, and P. Bertet¹
¹ *Quantronics Group, SPEC, IRAMIS, DSM, CEA Saclay, Gif-sur-Yvette, France and*
² *Forschungszentrum Jülich, Peter Grünberg Institut (PGI-2), 52425 Jülich, Germany*

We present measurements of superconducting flux qubits embedded in a three dimensional copper cavity. The qubits are fabricated on a sapphire substrate and are measured by coupling them inductively to an on-chip superconducting resonator located in the middle of the cavity. At their flux-insensitive point, all measured qubits reach an intrinsic energy relaxation time in the 6-20 μ s range and a pure dephasing time comprised between 3 and 10 μ s. This significant improvement over previous works opens the way to the coherent coupling of a flux-qubit to individual spins.

Electronic spins in semiconductors such as NV centers in diamond or phosphorus donors in silicon can reach coherence times up to seconds [1–3] and are therefore promising candidates for quantum information processing. However, the main obstacle to an operational spin-qubit quantum processor is the difficulty of coupling distant spins. To solve this issue, it has been proposed to couple each spin to a superconducting circuit which acts as a quantum bus and mediates the spin-spin interaction [4, 5]. This approach requires to reach the strong coupling regime where the coupling strength g between the spin and the circuit is larger than their respective decoherence rates. Among all superconducting circuits, the largest coupling constants could be obtained with flux qubits (FQ) [6–13] due to their large magnetic dipole. They can reach up to $g/2\pi \sim 100$ kHz for realistic parameters, which is much larger than the best reported spin decoherence rates. This brings a strong motivation for developing FQs with a coherence time $T_2 > 2/g \sim 4$ μ s.

FQ coherence times reported up to now are limited to $T_2 \lesssim 2\mu$ s, with a sizeable irreproducibility [10, 13]. The reasons for these relatively short coherence times are numerous but stem in part from the poor control of the electromagnetic environment of the qubit in previously used dc-SQUID readout setups [9–11]. A better control of the environment was recently demonstrated in the case of another superconducting qubit, the transmon, by using a three dimensional (3D) cavity that allows reading out the qubit and protecting it from spontaneous emission [9]. A natural question is therefore whether it is also possible to increase the coherence times of FQs and their reproducibility by using such a setup.

In this work, we present the first measurements of FQs in a 3D cavity. The six qubits measured reach reproducible coherence times T_2 between 2 and 8 μ s, which would be already sufficient to reach the strong coupling regime with a single spin. In addition, our results shed light on decoherence of FQs, giving evidence that charge noise is the dominant decoherence mechanism at their flux-insensitive point.

A scheme of the three dimensional cavity used in our experiment is shown in Fig. 1a. The cavity is made of copper to enable the application of an external magnetic

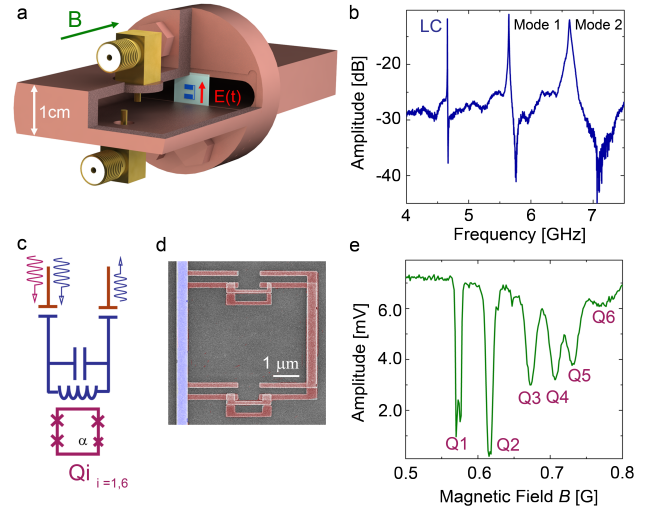


Figure 1: (a) Cut-away representation of the 3D cavity, with the LC circuit (in blue) on its sapphire chip. The green arrow represents the applied magnetic field B . The red arrow represents the ac electric field $E(t)$ of the first mode of the cavity. (b) Transmission spectrum of the cavity coupled to the LC resonator. The first peak at frequency $\omega_{LC}/2\pi = 4.643$ GHz corresponds to the resonance of the LC resonator while the two other peaks correspond to the first modes of the cavity. (c-d) Circuit diagram and colorized SEM micrograph showing the FQ (in red) inductively coupled to the LC resonator (in blue). (e) Amplitude of the transmitted signal at frequency ω_{LC} as a function of B , showing the signal from the six qubits.

field B to the FQs. Its dimensions are chosen for its first mode to be at 5.6 GHz. The sample inserted in the cavity is a sapphire chip with an LC resonator inductively coupled to six FQs, with a coupling constant ~ 50 MHz. The LC resonator acts as an intermediate coupler [12] between the FQs and the first cavity mode. It appears as a resonance peak at $\omega_{LC}/2\pi = 4.643$ GHz in the transmission spectrum (Fig. 1b) with a quality factor $Q_{LC} \sim 1.5 \times 10^4$ determined by the length of the input and output antennas inside the cavity (see Fig. 1a).

Figure 1d presents a colorized SEM micrograph of one of the FQs. It consists of a superconducting aluminum loop of area A intersected by four Josephson junctions.

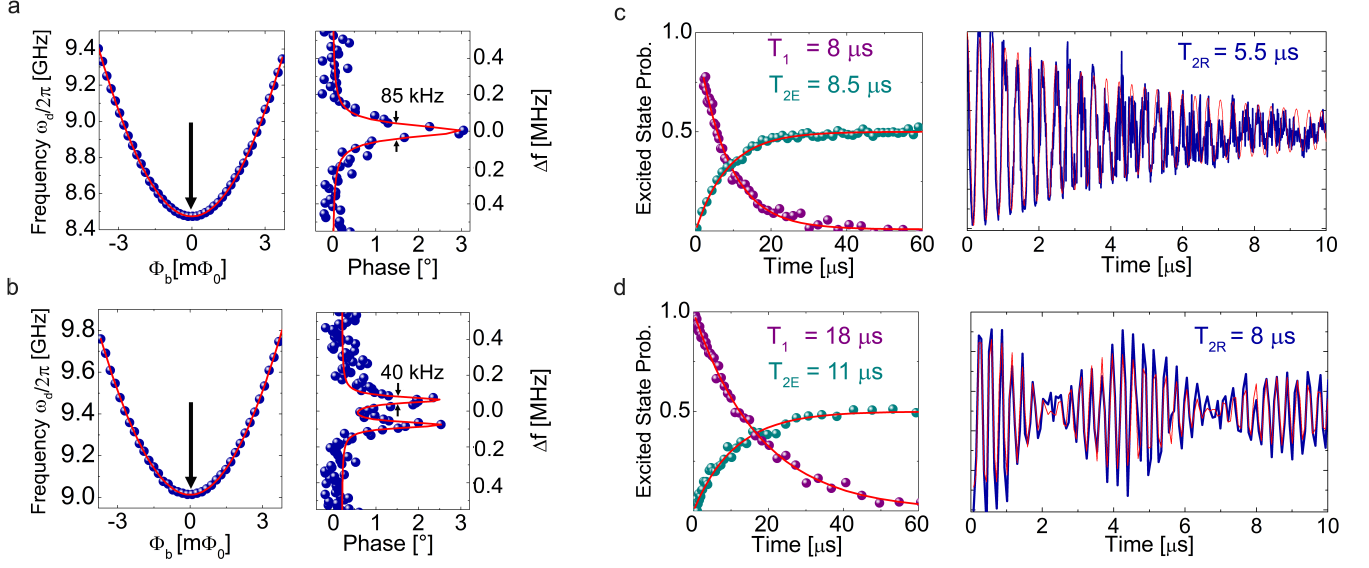


Figure 2: Characterisation of $Q3$ (top panels) and $Q4$ (bottom panels): (a-b) (left panels) Measured qubit frequency $\omega_{01}(\Phi_b)$ (blue dots) and fit (red curve) yielding the qubit parameters Δ and I_P . (Right panels) Spectroscopy data at $\Phi_b = 0$ (blue dots). $Q3$ spectrum is fitted with a single Lorentzian peak; $Q4$ spectrum is fitted with a sum of two Lorentzian peaks separated by 150kHz. (c-d) (left panels) Qubit energy relaxation and spin-echo measurements. The excited state probability is plotted as a function of the delay between the π pulse and readout pulse (blue dots) or between the two $\pi/2$ pulses of the echo sequence (purple dots). Red (orange) solid line is an exponential fit to the energy relaxation (spin-echo) data. (Right panels) Measured Ramsey fringes (blue solid line), with fit (red solid line) to exponentially damped single (top) and double (bottom) sine curves.

Three of the junctions are identical with a Josephson energy $E_J/h = 250$ GHz and a single electron charging energy $E_C/h = 3.6$ GHz; the fourth junction area is smaller than others by a factor α (see Table I). When the flux threading the loop $\Phi = BA$ is close to half a flux quantum $\Phi_0/2$, the two states characterized by a persistent current $\pm I_P$ in the loop become degenerate, hybridise and give rise to an energy splitting $\hbar\Delta$ called the flux-qubit gap. This circuit behaves therefore as a two-level system and its transition frequency is $\omega_{01} = \sqrt{\Delta^2 + \varepsilon^2}$ with $\varepsilon = 2I_P\Phi_b/\hbar$ and $\Phi_b = \Phi - \Phi_0/2$ [6, 7].

The qubits are fabricated by double angle-evaporation of Al–AlOx–Al on sapphire. We use a tri-layer PMMA–Ge–MAA process [18], which provides a good precision and reproducibility of the junction size and a rigid germanium mask, robust to the O_2 ashing and ion milling cleaning steps, which evacuates efficiently the charges during e-beam lithography. The measurements are performed in a cryogen-free dilution refrigerator at a temperature of 33 mK. The device is magnetically shielded with 2 Cryoperm boxes surrounding a superconducting enclosure. The cavity is also closed using Ecosorb corks and seals, in order to protect the sample from electromagnetic radiation that could generate quasiparticles [19]. The input line is attenuated at low temperature to minimize thermal noise and filtered with impedance-matched radiation-absorbing filters. The readout output line includes several filters, two isolators and a cryogenic HEMT

amplifier. Qubit state manipulations are performed by injecting in the input line microwave pulses at $\omega_d \sim \omega_{01}$, followed by a readout pulse at $\omega_m \sim \omega_{LC}$ whose amplitude and phase yield the qubit excited state probability [20].

An advantage of the cavity readout is the possibility to measure several qubits in a single run, by fabricating them with different loop areas A_i so that the field $B_i = \Phi_0/2A_i$ at which the flux reaches $\Phi_0/2$ is different for each qubit. Figure 1e presents the amplitude of the transmitted signal at frequency ω_{LC} as a function of B , showing a dip in the amplitude of the transmitted signal when the frequency of any of the six FQs comes close to ω_{LC} .

Each qubit is characterized by its spectroscopic parameters Δ and I_P , extracted from the dependence of its resonance frequency on the applied flux. These values, given in Table 1, are in good agreement with the predictions of the model described in [21] using both the measured values of α and of the tunnel resistance of the junctions. The coherence properties of each qubit are measured with the appropriate microwave pulse sequence [22]: the energy-relaxation time T_1 , the Ramsey coherence time T_{2R} from which one gets the Ramsey pure dephasing time $(T_{\varphi R})^{-1} = (T_{2R})^{-1} - (2T_1)^{-1}$, and the echo decay time T_{2E} yielding the echo pure dephasing time $(T_{\varphi E})^{-1} = (T_{2E})^{-1} - (2T_1)^{-1}$.

We now present detailed measurements on the qubits

Q3 and Q4 having the longest coherence times. The flux dependence of their frequency, shown in Fig.2a (b), yields $\Delta/2\pi = 8.47$ (9.01) GHz and $I_P = 169$ (160) nA for Q3 (Q4). Since both qubits were designed to have the same parameters, this shows good control of our e-beam lithography and oxidation parameters. We now turn to the coherence times at the so-called optimal point $\Phi_b = 0$, where the qubit frequency $\omega_{01} = \Delta$ is insensitive to first order to flux-noise [10, 11]. Energy relaxation (see Fig.2c-d) is exponential with $T_1 = 8 \mu\text{s}$ for Q3 and $18 \mu\text{s}$ for Q4. Ramsey fringes also show an exponential decay for Q3 with $T_{\varphi R} = 8.5 \mu\text{s}$, and an exponentially decaying beating pattern for Q4 with $T_{\varphi R} = 10 \mu\text{s}$. These features are consistent with the qubit spectra measured after an excitation pulse of $\sim 20 \mu\text{s}$ with a power well below saturation (see Fig.2a): Q3 line is Lorentzian with a full-width-half-maximum (FWHM) of 85 kHz, while Q4 line consists of a doublet of two Lorentzians separated by 150 kHz and having a width of 40 kHz, whose origin is discussed further below.

The amplitude of the spin-echo signal decays exponentially (see Fig.2 c,d) with finite pure dephasing times $T_{\varphi E} = 17 \mu\text{s}$ for Q3 and $T_{\varphi E} = 16 \mu\text{s}$ for Q4. This moderate improvement compared to the Ramsey pure dephasing times points out to the presence of high-frequency noise in our circuit in contrast to previous reports [11, 13]. We attribute this effect to fluctuations in the photon number (photon noise) of one or several cavity modes inducing fluctuations of the qubit frequency due to the dispersive shift [10, 23, 24]. This noise cannot be compensated by the echo protocol because its correlation time ($\sim 100 \text{ ns} - 1 \mu\text{s}$) given by the mode energy damping is shorter than the echo sequence duration. By plunging the antennas deeper in the cavity for reducing the cavity damping time, the observation of a lower T_{2E} confirms this explanation [23, 24]. Interestingly, removing the photon-noise contribution from the Ramsey pure dephasing time yields a “low-frequency Ramsey dephasing time” $(\tilde{T}_{\varphi R})^{-1} = (T_{\varphi R})^{-1} - (T_{\varphi E})^{-1}$ with $\tilde{T}_{\varphi R} = 16 \mu\text{s}$ for Q3 and $\tilde{T}_{\varphi R} = 30 \mu\text{s}$ for Q4. This one order of magnitude improvement compared to previous flux-qubit experiments that reported $\tilde{T}_{\varphi R}$ in the $0.2 - 2.5 \mu\text{s}$ range at the optimal point [10, 11, 13] is discussed later.

Away from the optimal point, decoherence is governed mainly by flux-noise in agreement with previous works [11, 13]. The Ramsey and spin-echo damping become Gaussian as $|\Phi_b|$ increases, which is characteristic of $1/f$ noise [25]. Fitting the Ramsey (or echo) envelope as $f_{R,E}(t) = e^{-t/(2T_1)} e^{-(\Gamma_{\varphi R,E} t)^2}$, we observe a linear dependence of $\Gamma_{\varphi R,E} = (T_{\varphi R,E})^{-1}$ on $|\Phi_b|$, with $\Gamma_{\varphi R} \sim 4.5 \Gamma_{\varphi E}$ (see Fig. 3), consistent with dephasing caused by flux-noise. Indeed, assuming a flux-noise power spectral density $S_\Phi(\omega) = A_\Phi/\omega$, one can show [11, 25] that $\Gamma_{\varphi E} = \sqrt{A_\Phi \ln 2} |\partial\omega_{01}/\partial\Phi_b|$ and $\Gamma_{\varphi R} = \sqrt{A_\Phi \ln(1/\omega_{IR} t)} |\partial\omega_{01}/\partial\Phi_b|$, with ω_{IR} an infrared cut-

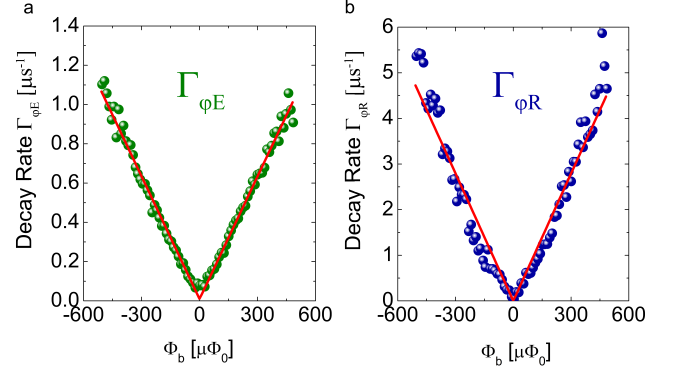


Figure 3: Pure dephasing rates of Q4 as a function of Φ_b : Experimental (dots) and fitted (line, see text) echo (a) and Ramsey (b) dephasing rates.

off frequency determined by the rate of data acquisition, and $|\partial\omega_{01}/\partial\Phi_b| \simeq 2 I_P |\varepsilon| / \hbar \Delta$. In our experiments, $\sqrt{\ln(1/\omega_{IR} t)} \sim 3.7$ predicting $\Gamma_{\varphi R} \sim 4.5 \Gamma_{\varphi E}$ in agreement with the measured value. We find an amplitude $A_\Phi = (2.5 \mu\Phi_0)^2$ comparable to previously reported values [11, 13].

All six qubits were characterized in this way, over several cooldowns (see Table I). Energy relaxation times were found to change from cooldown to cooldown, and also to occasionally change abruptly in the course of one cooldown. Several mechanisms contribute to relaxation; among them, spontaneous emission of a photon by the qubit in the measurement lines (the so-called Purcell regime [26]). Because this spontaneous emission rate T_P^{-1} is also the rate at which a photon coming from the measurement line is absorbed by the qubit, it can be quantitatively determined by measuring the qubit Rabi frequency Ω_R for a given microwave power P_{in} at the cavity input. For a qubit coupled symmetrically to the input and output lines, one gets

$$T_P = \frac{2}{\Omega_R^2} \frac{P_{in}}{\hbar \omega_{01}}. \quad (1)$$

	$\Delta/2\pi$ (GHz)	I_P (nA)	α	T_1 (μs)	T_P (μs)	$T_{\varphi R}$ (μs)	$T_{\varphi E}$ (μs)
Q1	2.70	245	0.61	6-10	1.1×10^5	2	7
Q2	4.91	207	0.55	2	3	-	-
Q3	8.47	169	0.49	6.5-8	30	8	17
Q4	9.01	160	0.49	13-18	270	10	16
Q5	9.71	171	0.43	5.5-12	90	5	>100
Q6	15.15	140	0.4	4	12	-	-

Table I: Parameters of the different measured FQs. Here Δ is the FQ gap, I_P is the persistent current flowing in the loop of the qubit, α corresponds to the measured ratio between the small and big junctions, T_1 is the relaxation time, T_P the Purcell limit time due to the coupling of the qubit with the cavity, $T_{\varphi R}$ and $T_{\varphi E}$ the coherence times obtained by Ramsey and Echo sequences respectively.

Comparing these estimates with the measured T_1 times (see Table I), we find that $Q2$ and $Q6$ are almost Purcell-limited. The intrinsic energy relaxation time $1/(T_1^{-1} - T_P^{-1})$ of all six measured qubits at their optimal point is thus in the $6 - 20 \mu\text{s}$ range. This significant improvement over previous reports of T_1 in the $0.5 - 4 \mu\text{s}$ range [9–11, 27] (except one sample for which $T_1 = 12 \mu\text{s}$ [13]) is probably due to a combination of several factors: good control of the electromagnetic environment in the 3D cavity [9], careful filtering and shielding against infrared radiation [19], low-loss sapphire substrate and different fabrication process.

The frequency dependence of the relaxation rate $\Gamma_1 = (T_1)^{-1}$ of $Q4$ in the vicinity of the optimal point is shown in Fig. 4. Large variations are observed, with in particular a reproducible increase of the relaxation rate by a factor 2 over 1 MHz, as also recently observed for a transmon qubit [28]. No corresponding anomaly in the Rabi frequency was observed at this point, which excludes spontaneous emission into the measurement lines (see Eq. (1)). We attribute therefore this peak to one resonant microscopic two-level system (TLS) weakly coupled to the qubit [28]. The remaining constant background $\sim (20 \mu\text{s})^{-1}$ could be due to dielectric losses, vortex motion, or out-of-equilibrium quasiparticles.

To estimate the quasiparticle contribution to relaxation, the same measurements were performed at 150 mK, a temperature at which the quasiparticle density is expected to be close to its thermal equilibrium value. The relaxation rate increases to $\Gamma_1^{(150 \text{ mK})} \simeq (5 \mu\text{s})^{-1}$ due to quasiparticles with a similar frequency dependence as at 33 mK, although less pronounced. Assuming that quasiparticles are mainly generated in the pads of the LC resonator and diffuse into the galvanically coupled qubits, we estimate the density of quasiparticles in the vicinity of the qubit $n_{qp}(150 \text{ mK}) = 1 \mu\text{m}^{-3}$ [29]. This density yields a theoretical relaxation rate $\Gamma_1^{(qp)} = (14 \mu\text{s})^{-1}$ [21], lower than the measured value by a factor 3, a discrepancy which we attribute to the crudeness of the modelling of quasiparticle diffusion. Since $\Gamma_1^{(qp)}$ is proportional to the quasiparticle density [29], we conclude that an out-of-equilibrium quasi-particle density of $\sim 0.3 \mu\text{m}^{-3}$ would be sufficient to explain the measured energy relaxation times at 33mK, which seems a plausible value in view of earlier reports in other superconducting qubit circuits [9–11]. However, the dielectric loss contribution is also important. Taking into account reported values of dielectric loss tangents $\sim 2 \times 10^{-5}$ [21], we find $\Gamma_1^{(dielectric)} \sim (25 \mu\text{s})^{-1}$, which is comparable to the measured values. Along these lines, we note that flux qubits fabricated on a high resistivity silicon chip and measured with the same setup at 33 mK showed a five-fold increase in relaxation rate.

Another interesting aspect of our experiment is the long Ramsey pure dephasing time $T_{\varphi R}$ measured for $Q3$

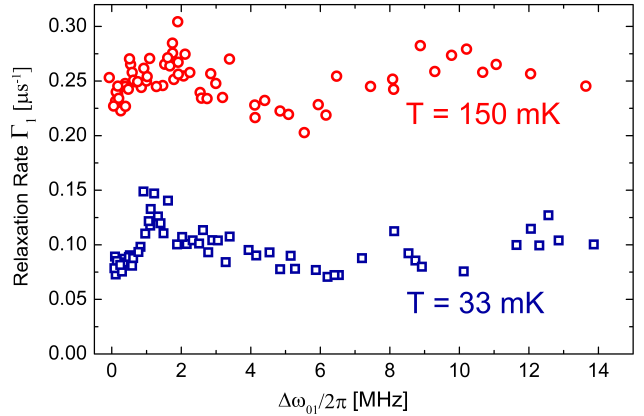


Figure 4: Frequency dependence of the relaxation rate Γ_1 of $Q4$ in the vicinity of its optimal point at $T = 33 \text{ mK}$ (blue squares) and $T = 150 \text{ mK}$ (red circles), showing an increased relaxation rate caused by quasi-particles.

and $Q4$ at their flux optimal point. Although not quite as long, all measured qubits have $T_{\varphi R}$ in excess of $3 \mu\text{s}$ (see Table I). The origin of decoherence at the optimal point for FQs has so far not been identified. One striking feature is the large variability of reported values of $T_{\varphi R}$ at the optimal point for rather similar FQ samples, ranging from $0.2 \mu\text{s}$ [10] up to $10 \mu\text{s}$ in this work, whereas $T_{\varphi R} = 2.5 \mu\text{s}$ in [13]. A doublet structure in the qubit line was frequently observed at the optimal point [10, 11, 31], with a greatly varying splitting (20 MHz in [10] and 150 kHz in this work, as seen in Fig. 2b) which was also found to vary in time.

All these features are consistent with charge noise being the dominant noise source limiting $T_{\varphi R}$ at the optimal point. The sensitivity to this noise is exponentially dependent on the ratio E_J/E_C [7] which is twice smaller in [10] compared to the present work. Using the model described in [21], we estimate a charge modulation amplitude of $\sim 50 \text{ kHz}$ for $Q3/Q4$ compared to $\sim 120 \text{ MHz}$ for [10] ($\sim 300 \text{ kHz}$ for [13]), yielding a three orders of magnitude lower charge noise sensitivity which explains qualitatively the difference in dephasing time. The doublet lineshape of $Q4$ can be attributed to slow fluctuations of the electron number parity on one of the qubit islands [31] as observed for transmon qubits [11, 32].

In conclusion, we have characterized the coherence properties of six FQs in a three-dimensional microwave cavity. We consistently find intrinsic energy relaxation times T_1 ranging between 6 and $20 \mu\text{s}$, a significant improvement over previous FQ measurements that we attribute to good control of the electromagnetic environment provided by the 3D cavity, low-loss substrate, and careful filtering. We identify weakly coupled two-level systems, quasiparticles and dielectric losses as likely sources of energy damping. At the optimal point, long Ramsey pure dephasing times up to $10 \mu\text{s}$ are measured,

limited by a combination of photon noise and charge noise with roughly equal contribution. We argue that charge noise is the dominant microscopic dephasing mechanism for FQs at the optimal point, and that its effect can be greatly minimized by choosing proper qubit parameters. Our results prove that FQs can reliably reach long coherence times, which opens new perspectives for the field of hybrid quantum circuits, in particular for the coherent coupling of single spins to superconducting circuits.

We would like to acknowledge fruitful discussions with M. Devoret, A. Lupascu and within the Quantronics group. We thank P. Sénat, P.-F. Orfila, D. Duet, J.-C. Tack, P. Pari, D. Bouville, P. Forget and M. de Combarieu for their technical support. This work was supported by the ANR CHIST-ERA project QINVC, the C’Nano IdF project QUANTROCRYO, the ERC project CIRQUSS, the JSPS and by the EU under REA Grant Agreement No. CIG-618258 (GC).

* Electronic address: michael.stern@cea.fr

- [1] N. Bar-Gill et al., *Nature Comm.*, **4**, 1743 (2013).
- [2] A. Morello et al., *Nature*, **467**, 687 (2010).
- [3] K. Saeedi et al., *Science*, **342**, 830 (2013).
- [4] D. Marcos et al., *Phys. Rev. Lett.*, **105**, 210501 (2010).
- [5] J. Twamley and S. D. Barrett, *Phys. Rev. B*, **81**, 241202 (2010).
- [6] J. E. Mooij et al., *Science*, **285**, 1036 (1999).
- [7] T. P. Orlando et al., *Phys. Rev. B*, **60**, 15398 (1999).
- [8] C. H. van der Wal et al., *Science*, **290**, 773 (2000).
- [9] I. Chiorescu, Y. Nakamura, C. J. P. M. Harmans, J. E. Mooij, *Science*, **299**, 1869 (2003).
- [10] P. Bertet et al., *Phys. Rev. Lett.*, **95**, 257002 (2005).
- [11] F. Yoshihara, K. Harrabi, A.O. Niskanen, Y. Nakamura, J.S. Tsai, *Phys. Rev. Lett.*, **97**, 167001 (2006).
- [12] P. Forn-Diaz et al., *Phys. Rev. Lett.*, **105**, 237001 (2010).
- [13] J. Bylander et al., *Nature Phys.*, **7**, 565 (2011).
- [14] X. Zhu et al., *Nature*, **478**, 221 (2011).
- [15] Y. Kubo et al., *Phys. Rev. Lett.* **107**, 220501 (2011).
- [16] H. Paik et al., *Phys. Rev. Lett.*, **107**, 240501 (2011).
- [17] I. Pop et al., *Nature*, **508**, 369 (2014).
- [18] J. Romijn and E. van der Drift, *Physica B* **152**, 14 (1988).
- [19] R. Barends et al., *APL* **99**, 113507 (2011).
- [20] A. Blais, R.S. Huang, A. Wallraff, S.M. Girvin & R.J. Schoelkopf, *Phys. Rev. A* **69**, 062320 (2004).
- [21] See Supplementary Materials.
- [22] D. Vion et al., *Science* **296**, 886 (2002).
- [23] C. Rigetti et al., *Phys. Rev. B*, **86**, 100506 (2012).
- [24] A.P. Sears et al., *Phys. Rev. B*, **86**, 180504(R) (2012).
- [25] G. Ithier et al., *Phys. Rev. B*, **72**, 134519 (2005).
- [26] A.A. Houck et al., *Phys. Rev. Lett.*, **101**, 080502 (2008).
- [27] J.E. Johnson, et al. *Phys. Rev. Lett.* **109**, 050506 (2012).
- [28] R. Barends et al., *Phys. Rev. Lett.*, **111**, 080502 (2013).
- [29] G. Catelani, R.J. Schoelkopf, M. H. Devoret & L.I. Glazman, *Phys. Rev. B* **84**, 064517 (2011).
- [30] P.J. de Visser et al., *Phys. Rev. Lett.* **106**, 167004 (2011).
- [31] M. Bal et al., arXiv:1406.7350 (2014).
- [32] J.A. Schreier et al., *Phys. Rev. B*, **77**, 180502 (2008).
- [33] D. Risté et al., *Nature Comm.* **4**, 1913 (2013).

Supplementary Materials

Appendix A: Hamiltonian of the 4-junction flux qubit

In this section, we present a model of a 4-junction flux qubit taking into account the main geometric capacitance terms and compare the calculation results with our experimental data.

Fig. 5a presents the circuit diagram of our model. The loop of the qubit is formed by four islands $I_{i=1,4}$ shown on Fig. 5b and connected by 4 Josephson junctions. Three junctions are identical while the area of the junction between islands I_1 and I_4 is smaller than the others by a factor α .

The full (4×4) geometric capacitance matrix of the circuit was calculated using a three-dimensional electromagnetic simulator [1]. We include in the diagram three capacitors which account for the main contribution of the geometric capacitance. Capacitor C_C represents the capacitance between the largest qubit island I_1 and I_3 ; the latter is connected galvanically to the pads of the LC resonator. Capacitors C_{g1} and C_{g3} are respectively the capacitances to ground of I_1 and I_3 .

For qubit Q4, the values of these capacitances were found to be $C_{g1} = 0.04$ fF, $C_{g3} = 477$ fF and $C_C = 0.57$ fF.

In the limit $C_{g3} \gg C_{g1}$ relevant to our experiment, the circuit Hamiltonian can be written as:

$$H = -E_J [\cos(\varphi_1) + \cos(\varphi_2) + \cos(\varphi_3) + \alpha \cos(\varphi_1 + \varphi_2 + \varphi_3 - 2\pi\Phi/\Phi_0)] \quad (A1)$$

$$+ 4E_C \frac{(1 + 2\alpha + 2c_r)n_1^2 + (1 + 2\alpha + c_r(1 + \alpha))(n_2^2 + n_3^2) - 2\alpha(n_1n_2 + n_1n_3 + n_2n_3) - 2c_r(1 + \alpha)n_2n_3}{1 + 3\alpha + 2c_r(1 + \alpha)}$$

where φ_i are the phase differences across the three large junctions of Josephson energy E_J , the operators n_i are conjugated to φ_i and count the number of Cooper pairs tunneling across the junctions, C is the capacitance of the large junctions, E_C is given by $E_C = \frac{e^2}{2C}$, c_r is a dimensionless parameter given by $c_r = \frac{C_C + C_{g1}}{C}$, Φ is the magnetic flux through the qubit loop, and Φ_0 is the magnetic flux quantum.

A complete description of the system includes all the inter-island capacitances, the capacitances to ground of the two small qubit islands and the inductance of the qubit loop. Assuming symmetry between the small islands, it can be shown [2] that the main effect of the additional capacitances is to slightly renormalize the parameters E_C , α , and c_r entering the charging energy part of Eq. (A1). In our numerical calculations we take this renormalization into account, using for the geometric capacitances the values extracted from the full capacitance matrix of our system but neglected the effect of the loop inductance.

We approximately solve the Schrödinger equation in the charge basis by truncating the Hilbert space to a large but finite number of charge states ($\sim 25^3$) and compare in Figs. c and d the results of the calculation to the measured values of the flux qubit gap Δ and persistent current I_P .

The Josephson energy E_J was estimated from Ambegaokar-Baratoff relation $E_J = h\Delta_0/(8e^2R_N)$ where Δ_0 is the superconducting gap of a 25-nm-thin aluminium film and R_N the tunneling resistance of the junction at low temperature and in the normal state. Assuming $\Delta_0 = 200 \mu\text{eV}$ [3] and measuring the room temperature tunneling resistance of the junctions, we find $E_J/h = 250 \pm 15$ GHz.

The charging energy of the junctions E_C was estimated by measuring their size and using standard values given in the literature for the capacitance per unit area. Assuming $c = 90 \pm 10$ fF/ μm^2 [4–6], we find $C = 5.4 \pm 0.6$ fF and $E_C/h = 3.6 \pm 0.4$ GHz.

The experimental data match well with the calculation and the major influence of adding the geometric capacitance terms is to reduce the flux qubit gap Δ by around 1 GHz.

Appendix B: Relaxation Rate Calculations

In this section, we discuss the calculations of the relaxation rates due to quasiparticles and dielectric losses; more details will be presented elsewhere [2].

Our estimate of the contribution $\Gamma_1^{(qp)}$ of quasiparticle tunneling to the relaxation rate of Q4 is based on the general theory of quasiparticle effects developed in Refs. [7, 8]. It was shown there that in a multi-junction qubit, $\Gamma_1^{(qp)}$ is obtained by summing the contributions of each individual junction, and that at low temperatures each term in the sum is proportional to the density of quasiparticles. A number of experiments [9–11] have shown that in aluminum devices at temperatures $\gtrsim 150$ mK, quasiparticles are in thermal equilibrium.

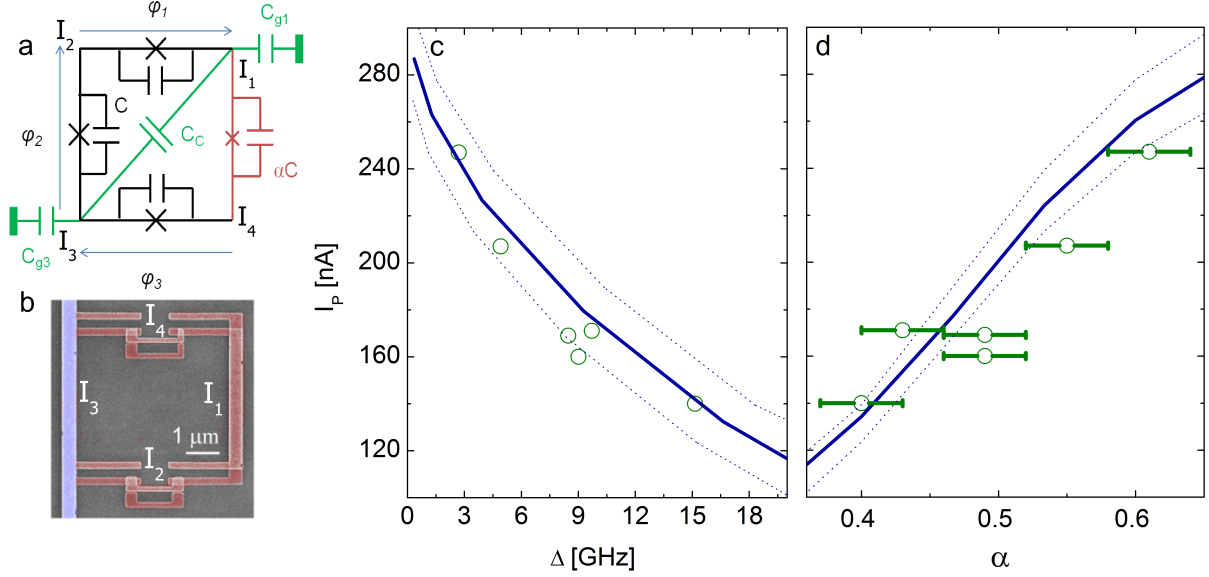


Figure 5: (a) Circuit diagram of the flux qubit including the main contributions of the geometric capacitance. (b) SEM micrograph of one of the flux qubits showing the different islands. The island I_3 (in blue) is connected galvanically to the pads of the LC resonator. (c) Persistent current I_P vs its gap Δ . For the blue solid line, the parameters of the model were $E_J/h = 250$ GHz, $E_C/h = 3.6$ GHz, $c_r = 0.1102$. The upper (lower) blue dotted line corresponds to $E_J/h = 265$ GHz and $E_C/h = 4$ GHz ($E_J/h = 235$ GHz and $E_C/h = 3.2$ GHz). The green circles are the experimental values. (d) Persistent current I_P vs α for the same parameters as (c). The horizontal error bars correspond to the confidence interval in the measure of α by SEM observation.

Based on the geometry of Q4, we estimate that at this temperature there are on average just 0.1 thermal quasiparticles in island I_1 . This means that the with high probability qubit decay can only be induced by a quasiparticle tunneling from the LC inductor galvanically connected to the qubit into one of the small island. Therefore, indicating with $x_{qp} = n_{qp}/2\nu_0\Delta_0$ the normalized quasiparticle density in the inductor (ν_0 is the aluminum density of states at the Fermi energy and $\Delta_0 = 200 \mu\text{eV}$), we have

$$\Gamma_1^{(qp)} \simeq \frac{4}{\pi} E_J x_{qp} \sqrt{\frac{2\Delta_0}{\omega_{01}}} \left[\left| \langle 1 | \sin \frac{\varphi_1}{2} | 0 \rangle \right|^2 + \left| \langle 1 | \sin \frac{\varphi_2}{2} | 0 \rangle \right|^2 \right] \quad (\text{B1})$$

The matrix elements can be estimated numerically after having obtained the approximate eigenstates of the Hamiltonian in Eq. (A1) and we find

$$\left| \langle 1 | \sin \frac{\varphi_1}{2} | 0 \rangle \right| \simeq \left| \langle 1 | \sin \frac{\varphi_2}{2} | 0 \rangle \right| \simeq 0.21 \quad (\text{B2})$$

Since in thermal equilibrium we have $x_{qp} = \sqrt{2\pi T/\Delta_0} e^{-\Delta_0/T}$, using the values $E_J = 250$ GHz and $\omega_{01} = 9.01$ GHz, from Eq. (B1) we arrive at the value $\Gamma_1^{(qp)} = 0.07 \mu\text{s}^{-1}$ reported in the main text. This calculation neglects completely the role of quasiparticles having tunneled into the other islands of the qubit and therefore underestimates $\Gamma_1^{(qp)}$.

Turning now our attention to the dielectric loss relaxation mechanism, we use Fermi's golden rule and the quantum fluctuation-dissipation relation to write each capacitor's C_i contribution to the decay rate in the form [2]

$$\Gamma_1^{C_i} = 16 \tan \delta_i E_{C_i} \sum_{j,k=1}^3 A_{ji} A_{ki} N_{jk} \quad (\text{B3})$$

where $\tan \delta_i$ is the inverse quality factor of the material causing the loss, the Hermitian matrix N_{jk} is defined, using the matrix elements of the number operators, as

$$N_{jk} = \langle 1 | n_j | 0 \rangle \langle 0 | n_k | 1 \rangle \quad (\text{B4})$$

and the dimensionless matrix A_{ij} accounts for the different coupling strengths between voltage fluctuations V_i in each capacitors and the number operators; specifically, this coupling adds the term

$$2e \sum_{i,j} n_j A_{ji} V_i \quad (\text{B5})$$

to the Hamiltonian in Eq. (A1).

For a simple order-of-magnitude estimate, we take the entries of matrix N_{ik} to be approximately identical

$$N_{ik} \approx 0.09 \quad (\text{B6})$$

with the numerical value calculated numerically using the (approximate) eigenstates of the Hamiltonian in Eq. (1). Then summing over indices j and k and over all four junctions, we find for the junction capacitors

$$\sum_{i \in J} E_{C_i} \sum_{j,k=1}^3 A_{ij} A_{ik} \simeq E_C \frac{(1 + 2c_r)^2 + 2 + \alpha(3 + c_r)^2}{[1 + 3\alpha + c_r(1 + \alpha)]^2} \quad (\text{B7})$$

Here we neglect for simplicity the renormalization of parameters, discussed above, due to the geometrical capacitances not included in the diagram of Fig. a. Similarly, summing over the geometric capacitors we get

$$\sum_{i \in G} E_{C_i} \sum_{j,k=1}^3 A_{ij} A_{ik} \simeq E_C \frac{4c_r}{[1 + 3\alpha + c_r(1 + \alpha)]^2} \quad (\text{B8})$$

From the measured decay rate at 33 mK, we can put upper bounds on the loss tangents for junction and ground capacitors; using Eqs. (B3) and (B7)-(B8). Assuming that the relaxation of the qubit would be due mainly to dielectric losses, we find

$$\tan \delta_J \sim 2.1 \times 10^{-6}, \quad (\text{B9})$$

and

$$\tan \delta_G \sim 2.4 \times 10^{-5}. \quad (\text{B10})$$

The value in Eq.(10) is an order of magnitude larger than recent estimates [12], where $\tan \delta_J \leq 3 \times 10^{-7}$ excluding the junction dielectric loss as the likely source of relaxation in our qubits. On the contrary, the number in Eq.(11) is close the the bound $\tan \delta_G \leq 2 \times 10^{-5}$ of Ref. [13], indicating that dielectric losses in the substrate or interface oxides can be one of the main sources of low-temperature relaxation. We note that similar experiments, realized in the same conditions but on a high-resistivity silicon chip, yielded an increased relaxation rate by a factor of ~ 5 .

* Electronic address: michael.stern@cea.fr

- [1] CST EM Studio, Computer Simulation Technology, <https://www.cst.com/Products/CSTEMS>.
- [2] G. Catelani, M. Stern, and P. Bertet, in preparation.
- [3] J. Aumentado et al., Phys. Rev. Lett., **92**, 066802 (2004).
- [4] L. J. Geerligs et al., Phys. Rev. Lett., **63**, 326 (1989).
- [5] V. Bouchiat, Ph.D thesis, SPEC-CEA Saclay(1998).
- [6] L. Bretheau, Ph.D thesis, SPEC-CEA Saclay (2013).
- [7] G. Catelani et al., Phys. Rev. Lett. **106**, 077002 (2011).
- [8] G. Catelani, R. J. Schoelkopf, M. H. Devoret, and L. I. Glazman, Phys. Rev. B **84**, 064517 (2011).
- [9] H. Paik et al., Phys. Rev. Lett., **107**, 240501 (2011).
- [10] P.J. de Visser et al., Phys. Rev. Lett., **106**, 167004 (2011).
- [11] D. Risté et al., Nature Com., **4**, 1913 (2013).
- [12] I. Pop et al., Nature, **508**, 369 (2014).
- [13] A. D. O'Connell et al., Appl. Phys. Lett., **92**, 112903 (2008).